

Highly polarized intrinsic emission and its orthogonal counterpart in Vela X-1

WANYUN WU ¹, FEI XIE ^{1,2}, LONG JI ³, MINGYU GE ^{4,5} AND FABIO LA MONACA ^{2,6}

¹*Guangxi Key Laboratory for Relativistic Astrophysics, School of Physical Science and Technology, Guangxi University, Nanning 530004, China*

²*INAF Istituto di Astrofisica e Planetologia Spaziali, Via del Fosso del Cavaliere 100, 00133 Roma, Italy*

³*School of Physics and Astronomy, Sun Yat-Sen University, Zhuhai, 519082, China*

⁴*Key Laboratory of Particle Astrophysics, Institute of High Energy Physics, Chinese Academy of Sciences, Beijing 100049, China*

⁵*University of Chinese Academy of Sciences, Chinese Academy of Sciences, Beijing 100049, China*

⁶*Dipartimento di Fisica, Università degli Studi di Roma “Tor Vergata”, Via della Ricerca Scientifica 1, 00133 Roma, Italy*

ABSTRACT

Vela X-1 is one of the most archetypal wind-fed X-ray pulsars (XRP), and the emergence of its orthogonal polarization states reveals distinctive polarimetric properties. Using data from Imaging X-ray Polarimetry Explorer (IXPE) observations of Vela X-1, we perform a polarization analysis of Vela X-1 using a triple power-law spectral model absorbed by varying column densities, successfully isolating two physically distinct orthogonal polarized components. The first polarized component corresponds to emission from the accretion mound surface that is not obscured by the wind clumps, with its polarization degree (PD) exceeding 30%. In specific phase intervals, the PD reaches $50.9 \pm 10.7\%$. This marks the first detection of such highly polarized neutron star emission in an XRP. The second polarized component likely originates from complex physical processes within or near the accretion mound, with its PD showing a potential negative correlation with column density. Furthermore, by rotating the predicted polarization angle (PA) of the first polarized component by 90° , we successfully achieve separate fitting and simultaneous fitting of the two orthogonal polarization states using the rotating vector model (RVM).

Keywords: binary star; polarization

1. INTRODUCTION

Accreting X-ray pulsars (XRP) are neutron stars (NS) in binary systems that accrete material from a companion star via an accretion disk or stellar wind. These systems are characterized by strong surface magnetic fields ($10^{12} \sim 10^{13}$ G) and exhibit a wealth of astrophysical phenomena governed by complex processes, including accretion flow transitions, plasma-magnetosphere interactions, and the variation of accretion geometry. X-ray polarization has emerged as a powerful probe of these phenomena (see recent review by Weng & Ji (2024)). The radiation from XRP is predicted to be highly polarized (e.g., Mészáros et al. (1988); Caiazzo & Heyl (2020)) due to the stark opacity contrast between the ordinary (O-mode) and ex-

traordinary (X-mode) photon propagation modes (Lai & Ho 2003). These modes arise from plasma effects and vacuum birefringence in ultra-strong magnetic fields (Gnedin 1974, 1978).

Recently, the Imaging X-ray Polarimetry Explorer (IXPE) (Soffitta et al. 2021; Weisskopf et al. 2022), launched in December 2021, has provided a dedicated instrument for studying the X-ray polarization properties of XRP. IXPE has observed some XRP, such as Her X-1 (Doroshenko et al. 2022; Akash et al. 2023; Heyl et al. 2024; Zhao et al. 2024), Cen X-3 (Tsygankov et al. 2022), 4U 1626–67 (Marshall et al. 2022), Vela X-1 (Forsblom et al. 2023, 2025), LS V+1477 (Doroshenko et al. 2023), GX 301–2 (Suleimanov et al. 2023), GRO J1008–57 (Tsygankov et al. 2023), X Persei (Mushtukov et al. 2023), EXO 2030+375 (Malacaria et al. 2023), Swift J0243.6+6124 (Poutanen et al. 2024b) and SMC X-1 (Forsblom et al. 2024). These systems exhibit a polarization degree (PD) significantly lower than tra-

ditional theoretical predictions, which is attributed to vacuum resonance in atmospheric temperature gradients or variations in viewing angle (Doroshenko et al. 2022). Among them, several wind-affected sources, such as LS V +44 17 and Vela X-1, show significant swings in polarization angle (PA), commonly attributed to the presence of dual-component polarization signatures.

As a typical wind-accretion source, Vela X-1 (4U 0900-40) is a high-mass X-ray binary (HMXB) located approximately at 2 kpc (Kretschmar et al. 2021) from Earth. It consists of a NS with a spin period of 283 seconds (McClintock et al. 1976) and its companion, the B0.5 Ia supergiant HD 77581 (Hiltner et al. 1972). The system has an orbital period of 8.964 days (Kreykenbohm et al. 2008), with the NS orbiting at a distance of about 1.7 times the radius of the supergiant (Quaintrell et al. 2003). Due to the nearly circular orbit ($e \sim 0.0898$) of the slowly rotating NS around its blue supergiant companion, the line-driven stellar wind provides a continuous source of material for accretion, with the companion’s mass-loss rate estimated at $10^{-6} M_{\odot} \text{ yr}^{-1}$ (G3mez-Garc3a et al. 2016). Although Vela X-1 exhibits a moderate intrinsic X-ray luminosity of approximately $4 \times 10^{36} \text{ erg s}^{-1}$ (Sato et al. 1986), its relative proximity makes it one of the brightest persistent X-ray sources in the sky. Consequently, it is one of the most extensively studied wind-accreting pulsars and is often regarded as the archetype of wind-fed HMXBs, where stellar wind accretion serves as the primary mechanism for mass transfer.

During the two observations by IXPE in 2022, Vela X-1 not only exhibits time-averaged low PD ($< 10\%$) but also shows a 90° PA swing between the high-energy and low-energy bands (Forsblom et al. 2023). In concurrent studies, Forsblom et al. (2025) proposed that the energy dependence of PD and PA can be modeled by the combination of a power-law component and a thermal bremsstrahlung component, which have different polarization properties with PA differing by 90° . At approximately 3.4 keV, the polarized flux contributions from these two components are equal, resulting in a net PD of zero. In addition, they proposed that the time-averaged low polarization and the presence of two orthogonal polarization states originate from the vacuum resonance under the atmospheric density gradient (Doroshenko et al. 2022), or the mixture of different emissions near the accretion mound.

In this paper, we mainly use a new composite spectral model to perform various polarization analyses of Vela X-1 with two IXPE observations. The structure of this paper is as follows. Section 2 describes the observations and data reduction procedures. The results

are presented in Section 3 and discussed in Section 4. Finally, we give the summary in Section 5.

2. OBSERVATION AND DATA REDUCTION

IXPE is a mission jointly initiated by NASA and the Italian Space Agency, launched on December 9, 2021. The detector consists of three identical grazing incidence telescopes and detector modules, each telescope includes an X-ray mirror assembly and a polarization-sensitive detector unit equipped with a Gas-Pixel detector, with an operational energy range of 2–8 keV (Soffitta et al. 2021; Di Marco et al. 2022a; Weisskopf et al. 2022). It is capable of performing imaging polarization measurements with a time resolution of better than 10 microseconds within the detector field of view of $12'.9 \times 12'.9$. A detailed description of the observatory and its performance can be found in Weisskopf et al. (2022) and reference therein.

Vela X-1 was observed twice by IXPE, with the observation periods being from April 15 to 21, 2022 (OBSID: 01002501) and from November 30 to December 6, 2022 (OBSID: 02005801). We downloaded the Level 2 dataset from HEASARC, and performed a solar system center correction on the photon arrival times, using the standard HEASoft (v.6.30.1) *barycorr*. To correct for orbital motion in the binary system, we used the orbital parameters for Vela X-1 provided by the Fermi Gamma-ray Burst Monitor. The pixel position offset correction and energy calibration were applied. In addition, we remove time intervals where the IXPE count rate in the background annular region was higher than the mean background value plus three times the root mean square (RMS) of this count rate, as these intervals are often considered to be affected by solar activities. After these processes, the source photons were extracted from a circular region with a radius of $70''$ centered on the source, and no background subtraction was applied, as suggested in Di Marco et al. (2023).

We process Level 2 data using version 30.2.32 of the *ixpeobssim* software package (Baldini et al. 2022), which incorporates the calibration database (v12) released on 17 November 2022. To derive polarization properties, we applied the PCUBE algorithm in *ixpeobssim* to generate polarization cubes, and utilized the PHA1, PHA1Q, and PHA1U algorithms to extract Stokes unweighted I , Q , and U spectra (Di Marco et al. 2022b), respectively. Then, the I spectrum was binned to ensure that each bin contained at least 30 counts, and then the same energy binning was applied to the Stokes Q and U spectra. The energy spectra were fitted in the XSPEC package (Arnaud 1996). In this paper, unless stated otherwise, uncertainties are reported at the 68% confidence level.

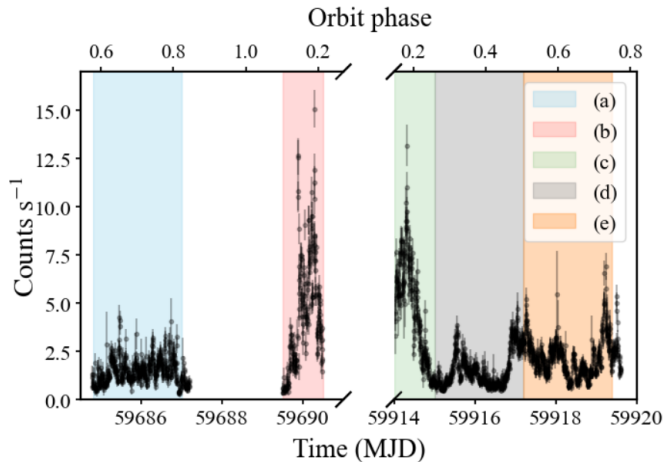


Figure 1. Light curves from the two IXPE observations of Vela X-1. Time intervals (a)–(e) are used for time-resolved polarization analysis, respectively corresponding to the MJD time intervals: (a) 59684.8–59687, (b) 59689.5–59690.5, (c) 59914–59915, (d) 59915–59917.2, and (e) 59917.2–59919.4.

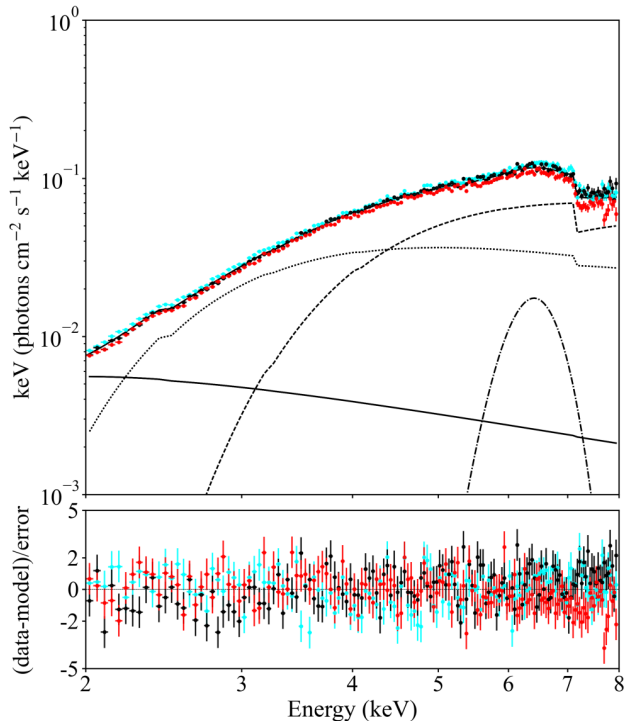


Figure 2. Top panel: the spectra of the combined dataset of two IXPE observations. The red, black and cyan colors represent the data from three DUs, respectively. The black solid line, dotted line, dashed line and dot–dashed line represent Component 1, Component 2, Component 3 and the Gaussian component of our fitting model, respectively. The fitting residuals are shown in the bottom panel.

3. RESULTS

The light curves of the two Vela X-1 observations obtained by IXPE in the 2–8 keV energy band are shown in Figure 1. We excluded the eclipse data (MJD 59687.3–59689.5) from the first observation in all subsequent analyses. The pulse phases were calculated using the ephemerides listed in Table 1 of Forsblom et al. (2023).

Subsequently, we present in this section the results of the time-averaged polarization analysis, the time-resolved polarization analysis, and the phase-resolved polarization analysis.

3.1. The triple power-law model and its polarization

The emission from wind-accreting X-ray pulsar systems strongly depends on the stellar wind and typically exhibits significant intrinsic flux variations. These variations cannot always be straightforwardly distinguished, particularly in the soft X-ray band (Diez et al. 2023). Therefore, we adopt a phenomenological model proposed by Mart’inez-N’unez et al. (2014), specifically a sum of three power-law components, to represent the combination of Vela X-1’s complex emission components. Each power-law has different normalizations but shares the same photon index, while being absorbed by distinct absorption components. This model was originally developed for the XMM-Newton spectrum of Vela X-1 in the 0.5–10 keV energy range, and was also used by Kretschmar et al. (2021) to investigate the impact of variable absorption on Vela X-1’s overall spectral shape.

Specifically, we implement the following model:

$$\begin{aligned} &const \times tbabs \times [polconst \times powerlaw \\ &+ polconst \times (tbabs \times powerlaw + tbabs \times powerlaw) \\ &+ polconst \times gauss], \end{aligned} \quad (1)$$

The *const* model represents cross-calibration constants. It accounts for calibration discrepancies between DUs, with DU1 fixed to unity in each observation.

We designate the first *powerlaw* component as Component 1 and the last two as Component 2,3. The *tbabs* model represents neutral hydrogen absorption, characterized by a single parameter: the equivalent hydrogen column density (N_{H}). We define N_{H} of the first *tbabs* model as $N_{\text{H},1}$, and fix it to the typical interstellar absorption value for Vela X-1 ($0.75 \times 10^{22} \text{ cm}^{-2}$, see van Genderen (1981)), implying that Component 1 remains unaffected by wind clumps and is solely absorbed by the interstellar medium. The subsequent two *tbabs* models are fitted freely, accounting for absorption by complex clumpy winds within the Vela X-1 system. We define them as $N_{\text{H},2}$ and $N_{\text{H},3}$.

Component	Parameter	01002501	02005801	Total
tbabs	$N_{H,1}$ (10^{22}cm^{-2})	[0.75]	[0.75]	[0.75]
	$N_{H,2}$ (10^{22}cm^{-2})	$8.4^{+1.1}_{-1.4}$	$7.9^{+0.7}_{-0.8}$	$8.1^{+0.6}_{-0.7}$
	$N_{H,3}$ (10^{22}cm^{-2})	$27.5^{+3.1}_{-3.0}$	27.0 ± 2.3	$27.0^{+1.9}_{-1.8}$
polconst	PD ₁ (%)	$41.9^{+19.0}_{-15.1}$	$30.4^{+6.5}_{-6.1}$	$32.6^{+6.1}_{-5.7}$
	PA ₁ (°)	35.6 ± 9.7	39.3 ± 5.4	38.3 ± 4.8
	PD _{2,3} (%)	6.0 ± 1.0	5.8 ± 0.8	5.9 ± 0.6
	PA _{2,3} (°)	-49.5 ± 5.1	-49.5 ± 4.0	-49.6 ± 3.2
powerlaw	Γ	2.16 ± 0.12	1.88 ± 0.08	1.94 ± 0.07
	Norm ₁	0.010 ± 0.002	0.018 ± 0.002	0.015 ± 0.001
	Norm ₂₊₃	$1.216^{+0.167}_{-0.114}$	$0.803^{+0.068}_{-0.053}$	$0.859^{+0.059}_{-0.048}$
gauss	E (keV)	$6.35^{+0.13}_{-0.11}$	6.39 ± 0.04	6.39 ± 0.04
	σ (keV)	[0.430]	[0.430]	[0.430]
	Norm	0.002	0.004	0.003
	$\chi^2/\text{d.o.f.}$	1568/1329	1450/1337	1541/1329

Table 1. Spectral parameters for each observation and the combined dataset in 2–8 keV energy range obtained by the spectropolarimetric analysis, as discussed in Section 3.1. Norm₂₊₃ denotes the total *powerlaw* normalization of Component 2,3, as defined in Section 3.1.

The *polconst* model, a multiplicative model describing constant polarization with energy, contains two parameters: PD and PA. Component 1 corresponds to an independent constant polarization component, while Component 2,3 share a common constant polarization component, representing the emission under the collective effect of wind clumps. Thus, we define the following parameter sets: PD₁ and PA₁ correspond to Component 1, PD_{2,3} and PA_{2,3} to Component 2,3.

Additionally, we include a Gaussian component to model the Fe K α line at 6.4 keV, consistent with previous studies (e.g., Fuerst et al. (2013), Grinberg et al. (2017), Diez et al. (2022), and Rahin & Behar (2023)). When the line parameters are left free during fitting, the best-fit solutions for both individual and combined datasets yield a line width smaller than IXPE’s energy resolution in the 6–7 keV range. Since such narrow widths cannot be reliably constrained by IXPE, we fix the Gaussian sigma to 0.43 keV. This corresponds to a full width at half maximum (FWHM) of 1.02 keV, matching IXPE’s FWHM resolution around 6.4 keV (Weisskopf et al. 2022).

The choice of 0.43 keV for the fixed sigma is supported by previous high-resolution studies. Fuerst et al. (2013) reported an orbitally averaged Fe K α line sigma of ≤ 0.7 keV using NuSTAR observations. Grinberg et al. (2017) found the line sigma varying between ~ 0.5 keV and 0.8 keV at orbital phases 0.21–0.25 with Chandra data, depending on flux hardness ratios. Rahin & Behar (2023) observed no significant orbital dependence in the Fe K α line flux. Collectively, these measurements support our adoption of 0.43 keV for the sigma parameter.

Furthermore, in our fitting procedures for all datasets, we first test free fitting with unconstrained Gaussian parameters. If the fitted Norm approaches zero, we fix both sigma and Norm to zero and refit to maintain model consistency throughout this work.

For the combined dataset from both observations, with sigma fixed at 0.43 keV, the fitted line centroid lies precisely at 6.4 keV. The F-test yields a value of 38.8 with a p-value less than 1×10^{-15} , and the differences in the Akaike Information Criterion (AIC) and Bayesian Information Criterion (BIC) are $\Delta\text{AIC} = -85.92$ and $\Delta\text{BIC} = -75.52$, respectively. These results strongly support the inclusion of the Gaussian component. Moreover, since the Gaussian iron line is expected to be unpolarized, we also assign a *polconst* to the Gaussian component and fix its PD to zero (see, e.g., Churazov et al. 2002; Veledina et al. 2024; La Monaca et al. 2024).

By freezing the *powerlaw* normalizations from the initial fit, convolving with the *cglumin* model, and refitting, we derive the unabsorbed luminosity in the 2–8 keV energy band. Subsequent analysis uses Norm₁ and Luminosity₁ for the *powerlaw* normalization and unabsorbed luminosity of Component 1, while Norm₂₊₃ and Luminosity_{2,3} denote the total *powerlaw* normalization and unabsorbed luminosity of Component 2,3.

Using XSPEC, we perform spectral fitting on the two IXPE observations of Vela X-1 in the 2–8 keV band. Additionally, we manually merge the spectra extracted from these two observations, obtain the total exposure time using XSELECT, and subsequently fit the merged spectrum. The best-fit spectrum for the combined dataset is shown in Figure 2. The results from

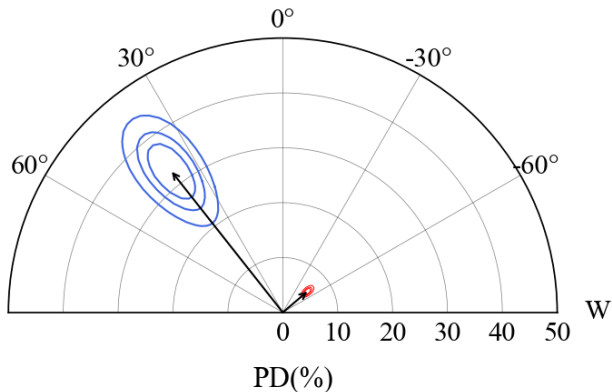


Figure 3. The polarization vectors of the combined dataset of two IXPE observations. The blue contours show the polarization vectors of Component 1, while the red shows the joint polarization vectors of Component 2,3. For each set of vectors, the three contours from outward to inward correspond to the 68.30%, 95.45%, and 99.73% confidence levels, respectively. Due to the narrow uncertainty ranges, the three red contours are visually indistinguishable at this scale.

fitting the datasets individually and the merged dataset are presented in Table 1.

As shown in Table 1, we find that both the second observation and the combined dataset exhibit significantly high PD_1 values, with significance levels of $\sim 5\sigma$. Additionally, PA_1 and $PA_{2,3}$ exhibit a 90° offset. The confidence contours for the polarization measurements were created by the *steppar* command in XSPEC and are shown in Figure 3 for the combined dataset.

We also attempt to separately compute the polarization of Component 1, Component 2, and Component 3 in the 2–8 keV energy band using XSPEC. We obtained $PD_1 = 14.6 \pm 9.0\%$, $PA_1 = 36.5 \pm 17.7^\circ$, $PD_2 = 1.4 \pm 3.0\%$ (consistent with zero), with PA_2 unconstrained, $PD_3 = 10.9 \pm 2.1\%$, and $PA_3 = -49.9 \pm 5.6^\circ$. The flux of Component 2 dominates in the 2.5–4 keV range, as shown in Figure 2. Moreover, the PA values of Component 1 and Component 3 exhibit an orthogonal trend, and their flux becomes comparable in the 3–4 keV energy band. Therefore, these can explain the zero degree of polarization around 3.5 keV reported in Forsblom et al. (2023). The 90° swing in PA between 2–3 keV and 4–8 keV mentioned in Forsblom et al. (2023) can also be explained by the polarization behavior of Component 1 and Component 3.

3.2. Time-resolved polarimetric analysis

To investigate temporal variations in spectral parameters and polarization properties, we partition the two observational datasets into five epochs: (a) to (e), as shown in Figure 1. Epochs (b) and (c) correspond to bright states within the orbits. To ensure sufficient pho-

ton counts, we set the duration of (b) and (c) to 1 day each and allocate 2.2 days to each of the remaining epochs. The final temporal segmentation is: (a) 59684.8–59687, (b) 59689.5–59690.5, (c) 59914–59915, (d) 59915–59917.2 and (e) 59917.2–59919.4. We subsequently fit the data from these five epochs using a methodology consistent with our previous analysis. The corresponding N_H , unabsorbed luminosity, polarization parameters, and Γ in the 2–8 keV energy range are tabulated in Table 2.

We observe that $N_{H,2}$ and $N_{H,3}$ fluctuate around $\sim 10 \times 10^{22} \text{ cm}^{-2}$ and $\sim 30 \times 10^{22} \text{ cm}^{-2}$, respectively, indicating absorption by a combination of distinct wind clumps. Additionally, across all epochs, PA_1 and $PA_{2,3}$ remain nearly orthogonal within errors or exhibit signs of orthogonality.

PD_1 consistently shows higher values in all epochs. Conversely, $PD_{2,3}$ is generally lower, consistent with the polarization values of Vela X-1 derived in previous research (Forsblom et al. 2023, 2025) and typical IXPE observational values for XRP (for a review, see Poutanen et al. (2024a)).

During epochs (c) and (d), we measure PD_1 values of $36.5 \pm 11.7\%$ and $33.2 \pm 8.4\%$ with significances of $> 3\sigma$. Additionally, $PD_{2,3}$ reaches its highest central values in epochs (c) and (d) at 7.1% and 7.2%, corresponding to significances of $\sim 3.6\sigma$ and $\sim 4.2\sigma$ respectively. Simultaneously, we find that $N_{H,2}$, $N_{H,3}$, and the photon index reach their lowest values during (c) and (d) across all epochs.

To further investigate factors influencing Vela X-1’s PD, we performed correlation analyses. Due to insufficient statistics PD_1 in epochs (a) and (b), we merely analyze the correlations between $PD_{2,3}$ and other spectral parameters. We find no correlation between $PD_{2,3}$ and $Luminosity_{2,3}$, but observe potential negative correlations with $N_{H,2}$ and $N_{H,3}$, showing Pearson coefficients of -0.740 and -0.716 (p -values = 0.153 and 0.174, respectively). These correlation results are shown in Figure 4.

3.3. Phase-resolved analysis of different components

The phase offset between the pulse profiles of the first and second observations was determined from cross-correlation (using the implementation provided by the Python library NumPy). Then, we divide the combined dataset of two observations into multiple phase intervals (each of width 0.2) and fit them with the method discussed in Section 3.1 in the 2–8 keV energy band using XSPEC. The derived parameters are shown in Table 3 and Figure 5.

MJD	Luminosity ₁ (10 ³⁵ erg s ⁻¹)	PD ₁ (%)	PA ₁ (°)	N _{H,2} (10 ²² cm ⁻²)	N _{H,3} (10 ²² cm ⁻²)	Luminosity _{2,3} (10 ³⁵ erg s ⁻¹)	PD _{2,3} (%)	PA _{2,3} (°)	Γ	χ ² / d.o.f.
(a)	0.05	32.1±18.1	51.7±16.1	13.6 ^{+1.4} _{-1.3}	34.8 ^{+5.5} _{-3.6}	2.48	6.0±1.3	-44.0±6.1	2.23	1483/1337
(b)	0.17	40.7±16.8	24.1±11.8	8.8±0.6	37.9 ^{+4.6} _{-3.9}	4.11	5.9±1.7	-59.2±8.4	2.28	1383/1337
(c)	0.53	36.5±11.7	41.9±9.4	5.4 ^{+0.9} _{-1.1}	26.5 ^{+4.6} _{-4.4}	4.82	7.1±2.0	-44.8±8.1	1.95	1347/1337
(d)	0.20	33.2±8.4	44.8±7.3	8.0 ^{+1.7} _{-1.5}	29.0 ^{+5.1} _{-3.0}	2.28	7.2±1.7	-53.1±6.7	1.68	1365/1337
(e)	0.08	45.4±17.1	20.4±10.8	12.9±0.8	35.5 ^{+5.1} _{-3.9}	3.76	4.1±1.0	-52.3±7.3	2.19	1397/1337

Table 2. Spectral parameters of different time intervals in 2–8 keV energy band obtained by the spectro-polarimetric analysis. In all time intervals, $N_{H,1}$ is fixed to the interstellar absorption value for Vela X-1 ($0.75 \times 10^{22} \text{ cm}^{-2}$). The unabsorbed luminosity of Component 1 and the total unabsorbed luminosity of Component 2,3 are also shown. (a)–(e) respectively correspond to the MJD time intervals: (a) 59684.8–59687, (b) 59689.5–59690.5, (c) 59914–59915, (d) 59915–59917.2, and (e) 59917.2–59919.4.

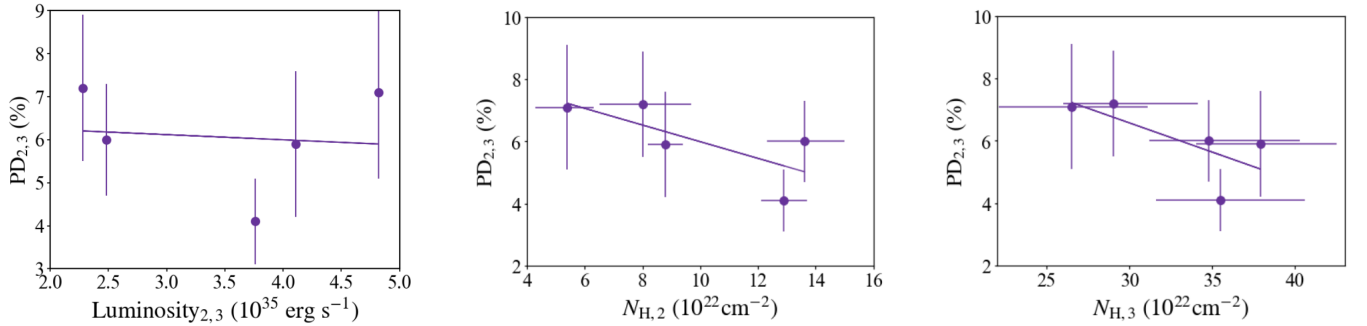


Figure 4. Correlation of parameters in Table 2. The left, middle and right panel respectively shows $PD_{2,3}$ versus $Luminosity_{2,3}$, $N_{H,2}$ and $N_{H,3}$.

We find that in the phase interval 0.2–0.4, PD_1 is detected at 50.9% with a significance of $\sim 5\sigma$. Additionally, the phase intervals 0.0–0.2 and 0.6–0.8 also show high PD_1 values of $34.7 \pm 11.6\%$ and $41.0 \pm 11.6\%$, corresponding to significances of $> 3\sigma$ and $\sim 4\sigma$ respectively.

We also find that $Luminosity_1$ and $Luminosity_{2,3}$ pulsate synchronously and vary in sync with the overall pulse profile, as shown in Figure 5(A) and (B). Additionally, Figure 5(B) reveals that Component 1 and Component 2,3 contribute to different parts of the total pulse profile, indicating that their emission regions and patterns may differ.

Additionally, Figure 5(D) shows that both PA_1 and $PA_{2,3}$ exhibit the same variation trend with phase and follow a sinusoidal pattern. The only exception is $PA_{2,3}$ in the 0.4–0.6 phase interval, which may result from the difficulty in constraining the PA due to the low significance of $PD_{2,3}$, or may indicate more complex polarization properties within the system. Overall, we can fit the Rotating Vector Model (RVM) to the pulse-phase dependent PA using the Rotating Vector Model (RVM) with the affine-invariant Markov Chain Monte Carlo (MCMC) ensemble sampler *emcee* in Python (Foreman-Mackey et al. 2012).

Previously, the RVM has been successfully applied to the phase-dependent PA variation in several X-ray

accreting pulsars (Doroshenko et al. 2022; Tsygankov et al. 2022; Mushtukov et al. 2023; Tsygankov et al. 2023; Malacaria et al. 2023; Doroshenko et al. 2023; Suleimanov et al. 2023; Heyl et al. 2024; Zhao et al. 2024; Poutanen et al. 2024b; Forsblom et al. 2024; Forsblom et al. 2025). In the RVM, if radiation escapes in the O-mode, PA can be described by the following equation (see Eq. (30) in Poutanen (2020)):

$$\tan(PA - \chi_p) = \frac{-\sin \theta \sin(\phi - \phi_0)}{\sin i_p \cos \theta - \cos i_p \sin \theta \cos(\phi - \phi_0)}, \quad (2)$$

where i_p is the inclination angle between the pulsar spin axis and the line of sight, θ is the magnetic obliquity (angle between the magnetic dipole and spin axis), χ_p is the pulsar position angle (measured from North to East), and ϕ_0 is the phase when the magnetic north pole crosses the observer’s meridian. When radiation escapes predominantly in the X-mode, the pulsar position angle becomes $\chi_p \pm 90^\circ$.

We first fit the RVM to PA_1 and $PA_{2,3}$ separately and constrain i_p to $73^\circ - 107^\circ$ based on Vela X-1’s orbital inclination limit (for a review, see Kretschmar et al. (2021)). We show covariance plots in Figures A1 and A2 and list resulting parameters in the first and second row of Table 4. Both solutions agree within errors.

Phase	Luminosity ₁ (10 ³⁵ erg s ⁻¹)	PD ₁ (%)	PA ₁ (°)	$N_{H,2}$ (10 ²² cm ⁻²)	$N_{H,3}$ (10 ²² cm ⁻²)	Luminosity _{2,3} (10 ³⁵ erg s ⁻¹)	PD _{2,3} (%)	PA _{2,3} (°)	Γ	$\chi^2/\text{d.o.f.}$
0.0–0.2	0.17	34.7±11.6	35.5±9.7	8.1 ^{+1.7} _{-1.5}	37.9 ^{+4.6} _{-3.9}	2.84	4.6±1.5	-66.8±9.7	1.91	1460/1337
0.2–0.4	0.18	50.9±10.7	29.9±6.0	8.7 ^{+1.5} _{-1.8}	28.9 ^{+5.5} _{-4.6}	2.94	12.2±1.5	-61.6±3.6	1.88	1311/1337
0.4–0.6	0.10	23.3±17.9	48.5±22.3	6.9 ^{+2.0} _{-1.6}	24.0 ^{+5.1} _{-2.5}	2.57	3.4±1.5	-3.6±13.5	2.17	1310/1337
0.6–0.8	0.18	41.0±11.6	48.5±8.1	8.9±0.9	30.3 ^{+3.8} _{-2.9}	4.07	9.4±1.2	-41.4±3.7	2.13	1475/1337
0.8–1.0	0.20	17.6±12.1	40.7±19.6	7.7 ^{+1.5} _{-1.4}	25.6 ^{+5.9} _{-3.4}	3.72	3.7±1.3	-44.3±10.7	1.96	1438/1337

Table 3. Pulse phase dependence of spectral parameters in 2–8 keV obtained by the spectro-polarimetric analysis, using the combined dataset of two IXPE observations. In all phase intervals, $N_{H,1}$ is fixed to the interstellar absorption value for Vela X-1 ($0.75 \times 10^{22} \text{ cm}^{-2}$).

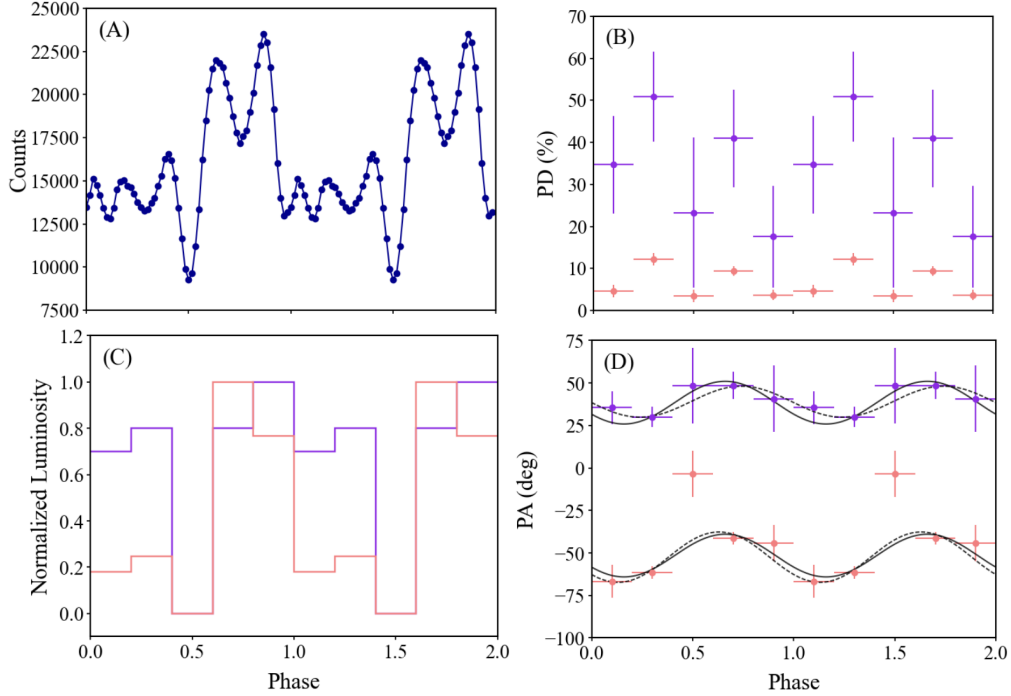


Figure 5. Results of the phase-resolved spectro-polarimetric analysis, using the combined dataset of two IXPE observations in 2–8 keV energy band. (A): The overall pulse profiles. (B): The phase-resolved PD₁ and PD_{2,3}. The purple line shows Component 1, and the light coral line shows Component 2,3. (C): Same colors indicate the variation of Luminosity₁ and Luminosity_{2,3}. (D): Same colors indicate the phase-resolved PA₁ and PA_{2,3}. The black solid curve shows the best-fit RVM for simultaneous fitting of PA₁ and PA_{2,3}. The black dashed curve represents the best-fit RVM for separate fitting of PA₁ and PA_{2,3}.

Subsequently, we simultaneously fit the RVM to PA₁ and PA_{2,3}. Prior to fitting, we applied an additional 90° rotation to the PA value predicted by the RVM for PA₁. Figure A3 shows covariance plots, while the third row of Table 4 presents parameters. The individual and joint fitting results are mutually consistent and align with the fitting outcomes obtained by Forsblom et al. (2025) using only high-energy segment data, showing a small magnetic obliquity angle θ and weak RVM constraints on i_p . We attempt to fix i_p to our obtained best-fit value and perform the fit again, but this can not yield any improvement in the fit.

4. DISCUSSION

In previous studies of Vela X-1 using a similar three power-law component model (Martínez-Núñez et al. 2014) to fit the *XMM-Newton* data in the 0.5–10 keV energy range, the authors proposed that the two most variable components across epochs correspond to two aspects of the emission from the NS surface. These exhibited characteristic N_H of $\sim 30 \times 10^{22} \text{ cm}^{-2}$ and $\sim 4 \times 10^{22} \text{ cm}^{-2}$. Another power-law might correspond to a soft excess below 3 keV caused by emission from photoionized or collisionally heated diffuse gas, or thermal emission from the neutron star surface (Hickox et al.

	i_p (deg)	θ (deg)	χ_p (deg)	$\phi_0/2\pi$
Component 1	$88.26^{+10.08}_{-10.04}$	$9.12^{+5.69}_{-5.36}$	$128.98^{+4.26}_{-4.29}$	$0.99^{+0.14}_{-0.14}$
Component 2,3	$90.18^{+8.92}_{-11.28}$	$14.81^{+4.61}_{-3.95}$	$127.49^{+2.67}_{-2.70}$	$0.88^{+0.06}_{-0.04}$
Total	$89.30^{+9.45}_{-10.69}$	$12.56^{+3.19}_{-2.82}$	$128.41^{+2.16}_{-2.22}$	$0.91^{+0.06}_{-0.05}$

Table 4. Best-fit RVM parameters for separate fitting and simultaneous fitting of PA₁ (corresponding to Component 1) and PA_{2,3} (corresponding to Component 2,3).

2004), with a N_H comparable to the interstellar absorption value, interpreted as a light echo in the distant stellar wind.

In our study, the 2–8 keV spectrum of Vela X-1 can also be fitted by the three power-law model. Figure 5(C) shows that the unabsorbed luminosities of Component 1 and Component 2,3 both vary approximately synchronously with the pulse. More importantly, the PA of these three components pulsates synchronously with the pulse phase, and the RVM fitting parameters are consistent with previous studies of Vela X-1 (Forsblom et al. 2025). This evidence implies that Component 1, like Component 2,3, originates from the polar cap emission of the neutron star rather than from the distant stellar wind.

Figure 5(B) reveals that Component 2,3 primarily contribute to the first minor peak of the total pulse profile, while Component 1 exhibits a relatively uniform contribution across the entire pulse profile. This implies distinct emission regions between the components. Given that Component 1 is only subject to interstellar absorption, we speculate that it represents emission from the surface layer of the accretion mound. Photons escaping this region do not traverse the main body of the accretion mound nor the accretion flow, but instead pass only through the uniform, optically thin stellar wind surrounding the neutron star periphery, experiencing minor absorption in distant media.

For neutron stars with strong magnetic fields in XRPs, the medium undergoes vacuum birefringence in the intense magnetic field, forming two polarization states: the O-mode and the X-mode (Gnedin 1974). Below the cyclotron resonance scattering energy (a fundamental energy around 25 keV and a first harmonic energy near 50 keV for Vela X-1, Staubert et al. (2018)), the opacity of the X-mode is much lower than that of the O-mode (Lai & Ho 2003). Therefore, the expected intrinsic radiation is predicted to be predominantly polarized in the X-mode, with predicted PD exceeding 30% across various models. Under high mass accretion rates, the PD may approach 80%. (for a review, see Poutanen et al. (2024a)).

Subsequently, this strongly polarized intrinsic radiation traverses the uniform, optically thin stellar wind surrounding the neutron star magnetosphere. For a uniform, spherically symmetric wind, the optical depth is estimated as $\tau_T \simeq 2 \times 10^{-4} \dot{M}_8 a_{12}^{-1} v_{x8}^{-1}$ (Kallman et al. 2015), where \dot{M}_8 is the mass-loss rate in units of $10^{-8} M_\odot \text{ yr}^{-1}$, a_{12} is the separation distance in 10^{12} cm, and v_{x8} is the wind velocity at the X-ray source in 10^3 km s^{-1} . For Vela X-1, adopting typical parameters $\dot{M}_8 = 1 \times 10^{-6}$ (Gimenez-García et al. 2016), $a_{12} = 3.55$ (Quaintrell et al. 2003), and an upper limit on orbital wind velocity $v_{x8} = 0.6$ (Kretschmar et al. 2021), we derive $\tau_T \sim 0.07$. At such a low optical depth, the PD remains nearly unchanged after scattering (Suleimanov et al. 2023).

This naturally explains the high PD of Component 1 we obtain. As shown in Table 3, PD₁ is detected with high significance ($\sim 5\sigma$) at approximately 50% ($50.9 \pm 10.7\%$). This marks the first detection of such highly polarized neutron star emission in an XRP with high significance.

For Component 2,3, considering their absorption by higher column densities, synchronous pulsation with Component 1, and primary contribution to the first minor peak of the total pulse profile, they likely represent neutron star emission originating from the high side of the accretion mound accumulation along the accretion flow direction. Component 2,3 may be absorbed by clumps of varying thicknesses, resulting in differences in column density. This implies structural differences in the accretion geometry on the neutron star surface, which further signifies variations in accretion rate.

The slightly absorbed Component 2 is only partially deflected and mixes with the original radiation, resulting in PD₂ = 0. In contrast, Component 3, which passes through a denser region, is almost completely deflected, with PA₃ showing an orthogonal trend relative to PA₁. This can explain the 90° swing in PA above and below 3.5 keV mentioned in Forsblom et al. (2023). The potential correlation between PD and column density suggests that vacuum resonance may occur within the accretion mound (Gnedin et al. 1978). In this resonance, the contributions of the plasma and magnetized vacuum

to the dielectric tensor cancel each other out, leading to rapid conversion between the X-mode and O-mode. If the region where final scattering occurs is also located in this area, significant Faraday depolarization may arise (Doroshenko et al. 2022). However, this requires the accretion mound to be sufficiently dense and accumulated in a region with a strong magnetic field (Pavlov & Shibano 1979). In any case, determining the specific physical mechanism will require future higher-precision polarization observations of Vela X-1.

The enhanced X-ray Timing and Polarimetry mission (eXTP) scheduled for launch in early 2030 offers the capability to perform high-resolution spectral, timing, and polarimetric observations within the 0.5–10 keV energy range (Ge et al. 2025). Therefore, we anticipate that eXTP will further validate the high polarization characteristics of Vela X-1 in this energy band and help us reach more definitive conclusions.

5. SUMMARY

The results of our study can be summarized as follows:

1. The IXPE spectrum of Vela X-1 is modeled by three power-law components with distinct equivalent hydrogen column densities and a Gaussian line at ~ 6.4 keV. Component 1 exhibits a constant polarization state with solely interstellar absorption. Component 2,3 share a constant polarization state but experience complex stellar wind absorption. These polarization states are mutually orthogonal.

2. The polarization state corresponding to the first power-law component exhibits a high PD ($\sim 30\text{--}50\%$) in time-averaged, time-resolved, and phase-resolved analyses, exceeding values commonly observed in HMXBs. Phase-resolved analysis measures $PD_1 \sim 50\%$ at $\sim 5\sigma$ significance. In contrast, $PD_{2,3}$ shows a lower PD ($\sim 5\%$).

3. Time-resolved analysis reveals that across all epochs, PA_1 and $PA_{2,3}$ remain nearly orthogonal within errors or exhibit signs of orthogonality. Additionally, when the photon index reaches its minimum, the detection significance of PD_1 increases, while $PD_{2,3}$ attains its maximum central values.

4. Correlation analysis reveals potential negative correlations between $PD_{2,3}$ and column density. No correlation exists between PD and Luminosity.

5. We apply the RVM to fit PA_1 and $PA_{2,3}$. By imposing a 90° offset on the pulsar position angle of Component 1, the derived pulsar geometric parameters were consistent with those obtained from fitting $PA_{2,3}$.

6. Due to its interstellar-level absorption column density and pulsating behavior, we conclude that Component 1 originates from the radiation emitted from the

accretion mound surface that is not obscured by the stellar wind. This radiation is dominated by a single polarization state in the strong magnetic field environment, with a high PD. Its polarization remains largely unchanged after traversing the optically thin outer stellar wind. This marks the first detection of such highly polarized neutron star emission in an XRP with high significance.

7. The low PD of Component 2,3 likely stems from complex physical processes in the vicinity of the accretion mound. Determining the specific mechanism will require future higher-precision polarization observations of Vela X-1.

ACKNOWLEDGMENTS

This work is supported by National Key R&D Program of China (grant No. 2023YFE0117200), and National Natural Science Foundation of China (grant No. 12373041, No. 12422306 and No. 12373051), and Bagui Scholars Program (XF). This work is also supported by the Guangxi Talent Program (“Highland of Innovation Talents”). This research used data products provided by the IXPE Team (MSFC, SSCC, INAF, and INFN) and distributed with additional software tools by the High-Energy Astrophysics Science Archive Research Center (HEASARC), at NASA Goddard Space Flight Center (GSFC). The Imaging X-ray Polarimetry Explorer (IXPE) is a joint US and Italian mission. FLM contribution is supported by the Italian Space Agency (Agenzia Spaziale Italiana, ASI) through contract ASI-INFN-2022-19-HH.0, by the Istituto Nazionale di Astrofisica (INAF) in Italy, and partially supported by MAECI with grant CN24GR08 “GRBAXP: Guangxi-Rome Bilateral Agreement for X-ray Polarimetry in Astrophysics”.

APPENDIX

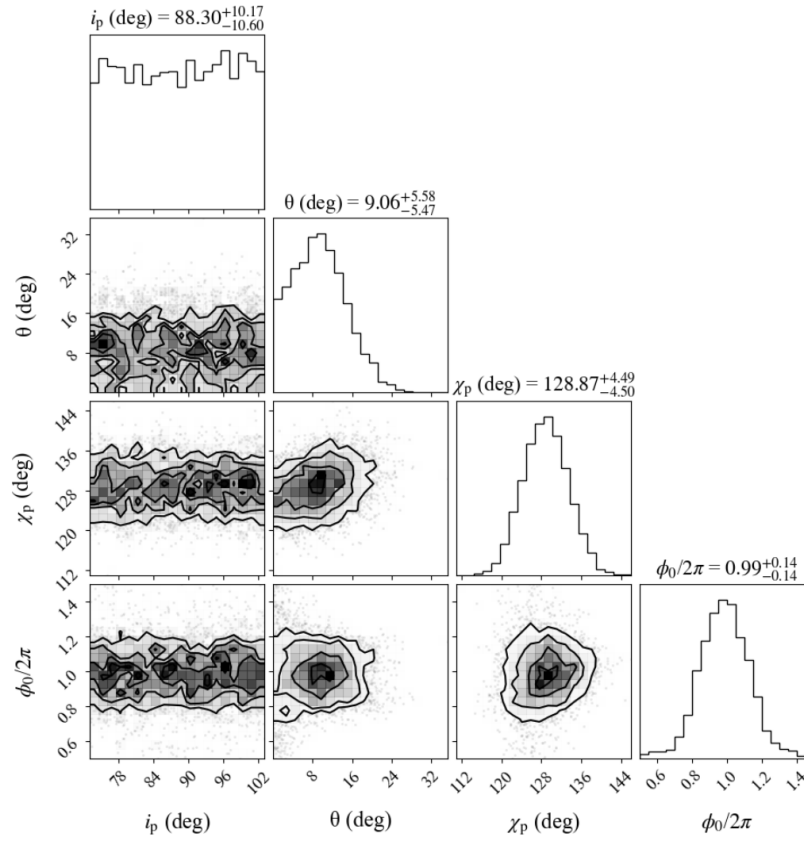


Figure A1. Corner plot of the posterior distribution for the parameters of RVM fitted to phase-resolved PA₁, as discussed in Section 3.3. The range of i_p is confined to 73°–107°. The two-dimensional contours correspond to 68.3%, 95.45% and 99.73% confidence levels. The histograms show the normalized one-dimensional distributions for a given parameter derived from the posterior samples.

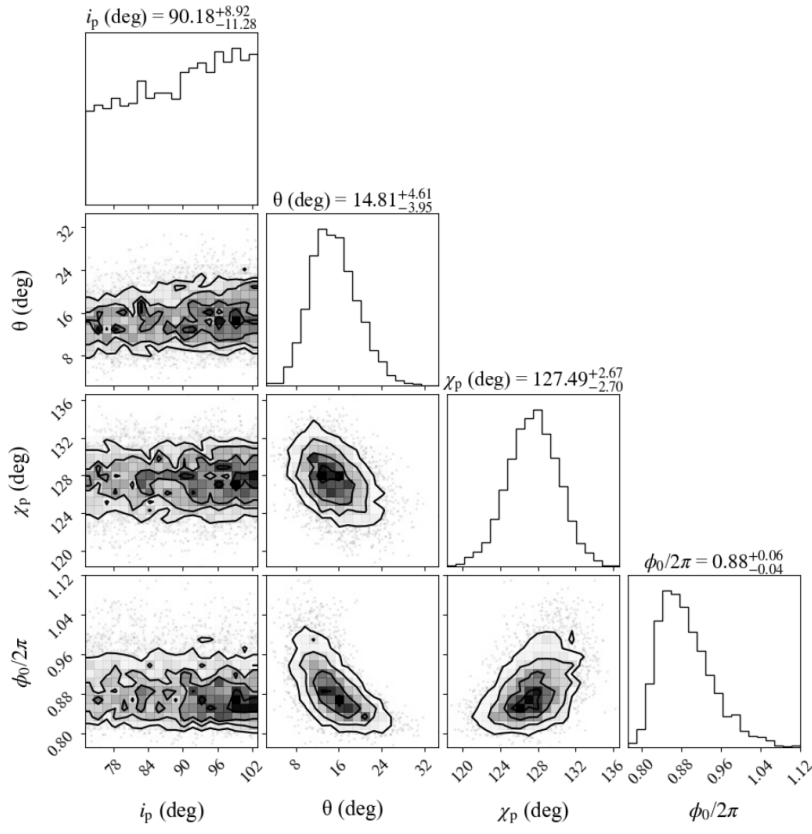


Figure A2. Same as Figure A1, but for phase-resolved PA_{2,3}

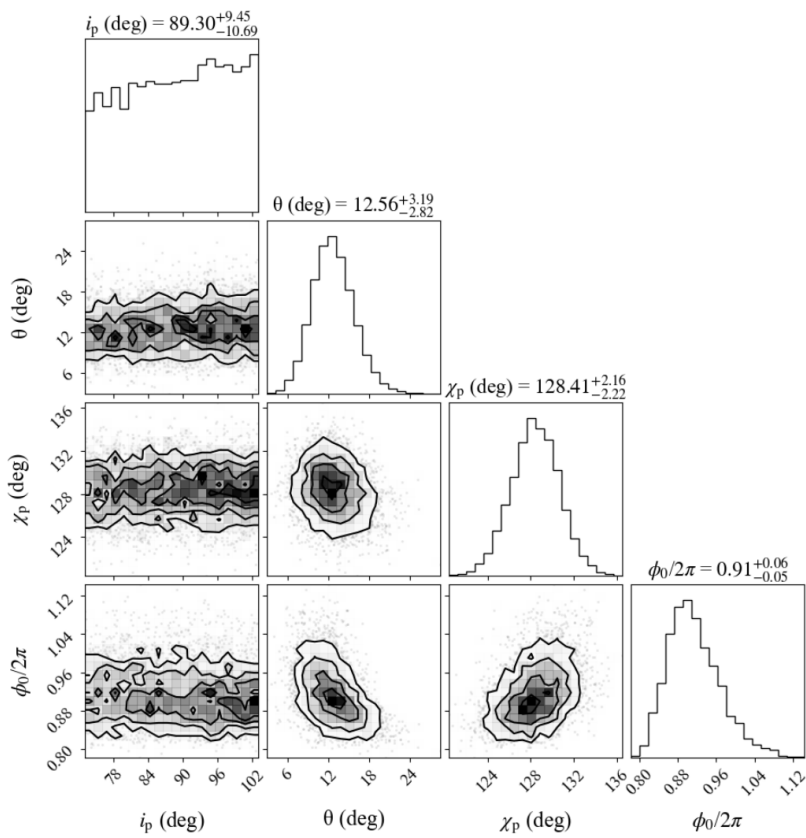


Figure A3. Same as Figure A1, but for the simultaneously fitting to phase-resolved PA₁ and PA_{2,3}

REFERENCES

- Akash, G., Divya, R., sand Méndez Mariano, B. Y., & Sudip, B. 2023, *The Astrophysical Journal Letters*, 948, doi: [10.3847/2041-8213/accffa](https://doi.org/10.3847/2041-8213/accffa)
- Arnaud, K. A. 1996, 101, 17
- Baldini, L., Bucciantini, N., Lalla, N. D., et al. 2022, *SoftwareX*, 19, 101194, doi: [10.1016/j.softx.2022.101194](https://doi.org/10.1016/j.softx.2022.101194)
- Caiazzo, I., & Heyl, J. S. 2020, *Monthly Notices of the Royal Astronomical Society*, doi: [10.1093/mnras/staa3428](https://doi.org/10.1093/mnras/staa3428)
- Churazov, E., Sunyaev, R., & Sazonov, S. 2002, *Monthly Notices of the Royal Astronomical Society*, 330, 817, doi: [10.1046/j.1365-8711.2002.05113.x](https://doi.org/10.1046/j.1365-8711.2002.05113.x)
- Di Marco, A., Fabiani, S., La Monaca, F., et al. 2022a, *AJ*, 164, 103, doi: [10.3847/1538-3881/ac7719](https://doi.org/10.3847/1538-3881/ac7719)
- Di Marco, A., Costa, E., Muleri, F., et al. 2022b, *AJ*, 163, 170, doi: [10.3847/1538-3881/ac51c9](https://doi.org/10.3847/1538-3881/ac51c9)
- Di Marco, A., Soffitta, P., Costa, E., et al. 2023, *The Astronomical Journal*, 165, doi: [10.3847/1538-3881/acba0f](https://doi.org/10.3847/1538-3881/acba0f)
- Diez, C. M., Grinberg, V., Furst, F., et al. 2022, *Astronomy & Astrophysics*, doi: [10.1051/0004-6361/202141751](https://doi.org/10.1051/0004-6361/202141751)
- . 2023, *Astronomy & Astrophysics*, doi: [10.1051/0004-6361/202245708](https://doi.org/10.1051/0004-6361/202245708)
- Doroshenko, V., Poutanen, J., Tsygankov, S. S., et al. 2022, *Nature Astronomy*, 6, 1433 , doi: [10.1038/s41550-022-01799-5](https://doi.org/10.1038/s41550-022-01799-5)
- Doroshenko, V., Poutanen, J., Heyl, J. S., et al. 2023, *Astronomy & Astrophysics*, doi: [10.1051/0004-6361/202347088](https://doi.org/10.1051/0004-6361/202347088)
- Foreman-Mackey, D., Hogg, D. W., Lang, D., & Goodman, J. B. 2012, *Publications of the Astronomical Society of the Pacific*, 125, 306 , doi: [D10.1086/670067](https://doi.org/10.1086/670067)
- Forsblom, S. V., Tsygankov, S. S., Suleimanov, V. F., Mushtukov, A. A., & Poutanen, J. 2025, *A&A*, 696, A224, doi: [10.1051/0004-6361/202553867](https://doi.org/10.1051/0004-6361/202553867)
- Forsblom, S. V., Poutanen, J., Tsygankov, S. S., et al. 2023, *The Astrophysical Journal Letters*, 947, L20, doi: [10.3847/2041-8213/acc391](https://doi.org/10.3847/2041-8213/acc391)
- Forsblom, S. V., Tsygankov, S. S., Poutanen, J., et al. 2024, *Astronomy & Astrophysics*, doi: [10.1051/0004-6361/202450937](https://doi.org/10.1051/0004-6361/202450937)
- Furst, F., Pottschmidt, K., Wilms, J., et al. 2013, *The Astrophysical Journal*, 780, doi: [10.1088/0004-637X/780/2/133](https://doi.org/10.1088/0004-637X/780/2/133)
- Ge, M., Ji, L., Taverna, R., et al. 2025
- Giménez-García, A., Shenar, T., Torrejón, J. M., et al. 2016, arXiv: High Energy Astrophysical Phenomena, doi: [10.1051/0004-6361/201527551](https://doi.org/10.1051/0004-6361/201527551)
- Gnedin, I. N., Pavlov, G. G., & Shibano, I. A. 1978, *Pisma v Astronomicheskii Zhurnal*, 4, 214
- Gnedin, Y. 1974, *Sov. J. Exp. Theor. Phys.*, 38, 903
- . 1978, *Sov. Astron. Lett.*, 4, 117
- Grinberg, V., Hell, N., Mellah, I. E., et al. 2017, arXiv: High Energy Astrophysical Phenomena, doi: [10.1051/0004-6361/201731843](https://doi.org/10.1051/0004-6361/201731843)
- Heyl, J. S., Doroshenko, V., González-Caniulef, D., et al. 2024, *Nature Astronomy*, doi: [10.1038/s41550-024-02295-8](https://doi.org/10.1038/s41550-024-02295-8)
- Hickox, R. C., Narayan, R., & Kallman, T. R. 2004, *The Astrophysical Journal*, 614, 881 , doi: [10.1086/423928](https://doi.org/10.1086/423928)
- Hiltner, W. A., Werner, J., & Osmer, P. 1972, *The Astrophysical Journal*, doi: [10.1086/180976](https://doi.org/10.1086/180976)
- Kallman, T. R., Dorodnitsyn, A. V., & Blondin, J. M. 2015, *The Astrophysical Journal*, 815, doi: [10.1088/0004-637X/815/1/53](https://doi.org/10.1088/0004-637X/815/1/53)
- Kretschmar, P., Mellah, I. E., Mart'inez-N'unez, S., et al. 2021, *Astronomy and Astrophysics*, doi: [10.1051/0004-6361/202040272](https://doi.org/10.1051/0004-6361/202040272)
- Kreykenbohm, I., Wilms, J., Kretschmar, P., et al. 2008, *Astronomy & Astrophysics*, 492, 511, doi: [10.1051/0004-6361:200809956](https://doi.org/10.1051/0004-6361:200809956)
- La Monaca, F., Di Marco, A., Ludlam, R. M., et al. 2024, *A&A*, 691, A253, doi: [10.1051/0004-6361/202451966](https://doi.org/10.1051/0004-6361/202451966)
- Lai, D., & Ho, W. C. G. 2003, *Phys. Rev. Lett.*, 91, 071101, doi: <https://doi.org/10.1103/PhysRevLett.91.071101>
- Malacaria, C., Heyl, J., Doroshenko, V., et al. 2023, *Astronomy & Astrophysics*, 675, A29, doi: [10.1051/0004-6361/202346581](https://doi.org/10.1051/0004-6361/202346581)
- Marshall, H. L., Ng, M., Rogantini, D., et al. 2022, *The Astrophysical Journal*, 940, 70, doi: [10.3847/1538-4357/ac98c2](https://doi.org/10.3847/1538-4357/ac98c2)
- Mart'inez-N'unez, S., Torrej'on, J. M., Kuhnel, M., et al. 2014, *Astronomy and Astrophysics*, 563, doi: [10.1051/0004-6361/201322404](https://doi.org/10.1051/0004-6361/201322404)
- McClintock, J. E., Rappaport, S., Joss, P. C., et al. 1976, *The Astrophysical Journal*, doi: [10.1086/182142](https://doi.org/10.1086/182142)
- Mészáros, P., Novick, R., Szentgyorgyi, A., Chanan, G. A., & Weisskopf, M. C. 1988, *The Astrophysical Journal*, 324, 1056, doi: [10.1086/165962](https://doi.org/10.1086/165962)
- Mushtukov, A. A., Tsygankov, S. S., Poutanen, J., et al. 2023, *Monthly Notices of the Royal Astronomical Society*, doi: [10.1093/mnras/stad1961](https://doi.org/10.1093/mnras/stad1961)
- Pavlov, G. G., & Shibano, Y. A. 1979, *Journal of Experimental and Theoretical Physics*, 49, 1457
- Poutanen, J. 2020, *Astronomy & Astrophysics*, doi: [10.1051/0004-6361/202038689](https://doi.org/10.1051/0004-6361/202038689)
- Poutanen, J., Tsygankov, S. S., & Forsblom, S. V. 2024a, *Galaxies*, doi: [10.3390/galaxies12040046](https://doi.org/10.3390/galaxies12040046)

- Poutanen, J., Tsygankov, S. S., Doroshenko, V., et al. 2024b, *Astronomy & Astrophysics*, doi: [10.1051/0004-6361/202450696](https://doi.org/10.1051/0004-6361/202450696)
- Quaintrell, H., Norton, A. J., Ash, T. D. C., et al. 2003, *Astronomy and Astrophysics*, 401, 313, doi: [10.1051/0004-6361:20011122](https://doi.org/10.1051/0004-6361:20011122)
- Rahin, R., & Behar, E. 2023, *The Astrophysical Journal*, 950, doi: [10.3847/1538-4357/acc386](https://doi.org/10.3847/1538-4357/acc386)
- Sato, N., Hayakawa, S., Nagase, F., et al. 1986, *Publications of the Astronomical Society of Japan*, 38, 731
- Soffitta, P., Baldini, L., Bellazzini, R., et al. 2021, *The Astronomical Journal*, 162, doi: [10.3847/1538-3881/ac19b0](https://doi.org/10.3847/1538-3881/ac19b0)
- Staubert, R., Trümper, J., Kendziorra, E., et al. 2018, *Astronomy & Astrophysics*, doi: [10.1051/0004-6361/201834479](https://doi.org/10.1051/0004-6361/201834479)
- Suleimanov, V. F., Forsblom, S. V., Tsygankov, S. S., et al. 2023, *Astronomy & Astrophysics*, doi: [10.1051/0004-6361/202346994](https://doi.org/10.1051/0004-6361/202346994)
- Tsygankov, S. S., Doroshenko, V., Poutanen, J., et al. 2022, *The Astrophysical Journal Letters*, 941, doi: [10.3847/2041-8213/aca486](https://doi.org/10.3847/2041-8213/aca486)
- Tsygankov, S. S., Doroshenko, V., Mushtukov, A. A., et al. 2023, *Astronomy & Astrophysics*, doi: [10.1051/0004-6361/202346134](https://doi.org/10.1051/0004-6361/202346134)
- van Genderen, A. M. 1981, *Astronomy and Astrophysics*, 96, 82
- Veledina, A., Muleri, F., Poutanen, J., et al. 2024, *Nature Astronomy*, 8, 1031, doi: [10.1038/s41550-024-02294-9](https://doi.org/10.1038/s41550-024-02294-9)
- Weisskopf, M. C., Soffitta, P., Baldini, L., et al. 2022, *Journal of Astronomical Telescopes, Instruments, and Systems*, 8, 026002, doi: [10.1117/1.JATIS.8.2.026002](https://doi.org/10.1117/1.JATIS.8.2.026002)
- Weng, S.-S., & Ji, L. 2024, *Universe*, doi: [10.3390/universe10120453](https://doi.org/10.3390/universe10120453)
- Zhao, Q. C., Li, H. C., Tao, L., et al. 2024, *Monthly Notices of the Royal Astronomical Society*, 531, 3935, doi: [10.1093/mnras/stae1173](https://doi.org/10.1093/mnras/stae1173)